Generalized Aubry-André-Harper model with modulated hopping and *p*-wave pairing

M. Yahyavi,[1,*] B. Hetényi,[1,2,†] and B. Tanatar[1,‡]

[1]*Department of Physics, Bilkent University, TR-06800 Bilkent, Ankara, Turkey*

[2]*Department of Theoretical Physics and MTA-BME "Momentum" Topology and Correlation Research Group, Budapest University of Technology and Economics, 1521 Budapest, Hungary*

(Received 23 April 2019; revised manuscript received 9 July 2019; published 12 August 2019)

We study an extended Aubry-André-Harper model with simultaneous modulation of hopping on-site potential and *p*-wave superconducting pairing. For the case of commensurate modulation of $\beta = 1/2$ it is shown that the model hosts four different types of topological states: Adiabatic cycles can be defined which pump particles two types of Majorana fermions or Cooper pairs. In the incommensurate case we calculate the phase diagram of the model in several regions. We characterize the phases by calculating the mean inverse participation ratio and perform multifractal analysis. In addition we characterize whether the phases found are topologically trivial or not. We find an interesting critical extended phase when incommensurate hopping modulation is present. The rise between the inverse participation ratio in regions separating localized and extended states is gradual rather than sharp. When in addition the on-site potential modulation is incommensurate we find several sharp rises and falls in the inverse participation ratio. In these two cases all different phases exhibit topological edge states. For the commensurate case we calculate the evolution of the Hofstadter butterfly and the band Chern numbers upon variation of the pairing parameter for zero and finite on-site potential. For zero on-site potential the butterflies are triangularlike near zero pairing when gap closure occurs they are squarelike and hexagonal-like for larger pairing but with the Chern numbers switched compared to the triangular case. For the finite case gaps at quarter and three-quarters filling close and lead to a switch in Chern numbers.

DOI: 10.1103/PhysRevB.100.064202

I. INTRODUCTION

The physics of Anderson delocalization-localization (or metal-insulator) transition in disordered fermionic systems is a problem of long-standing interest in condensed matter physics [1–3]. In one dimension uncorrelated random potentials lead to complete localization of all eigenfunctions [4,5], while mobility edges and the delocalization-localization transition will typically appear in 3D disordered systems. However, mobility edges may occur in some 1D systems [6–8], if the disorder distribution is deterministic, rather than uncorrelated. The paradigm of this class of quasiperiodic systems, incommensurate lattices (the superposition of two periodic lattices with incommensurate periods) is the Aubry-André model [9], or its two-dimensional analog, the Harper-Hofstadter model [10,11]. The delocalization-localization transition due to the disordered on-site potential can appear in the Aubry-André model when the lattice is incommensurate, arising from the self-duality of this model [12].

The model was explored [13–15] from a topological perspective. In the Aubry-André model with *p*-wave superconducting (SC) pairing the connection between the Su-Schrieffer-Heeger–like [16] and the Kitaev-like [17,18] topological phases was investigated [19]. Other studies [20–23] focused on localization effects. In addition, commensurate and incommensurate modulations may appear in on-site and hopping terms; the interplay between the two was studied in Ref. [24]. When hopping modulations are incommensurate [25], the system will go through Anderson-like localization, but no mobility edge is found. For commensurate hopping modulations topological zero-energy edge modes are found [25,26]. In Ref. [24] the incommensurate and commensurate off-diagonal modulations were combined resulting in the conclusion that the states depend on the phase between the two. Experimentally the model was realized in ultracold atoms in optical lattices [27,28] and in photonic crystals [29,30]. A recent experiment [13] realized the topological edge state.

In this paper, we study a generalized AAH model with modulated on-site potential, hopping, and *p*-wave pairing. For the bipartite case ($\beta = 1/2$) we show that four different topological excitations are possible. The same model, but without modulation of the *p*-wave pairing, was studied by Zeng *et al.* [19] and Liu *et al.* [23]. They studied both the commensurate and incommensurate cases. They mapped the phase diagram of the model, studied localization by investigating the mean inverse participation ratio (MIPR), and did multifractal analysis in the incommensurate case and showed the existence of topological edge states in the commensurate case. We also do these calculations for the model with modulated *p*-wave pairing. The MIPR studies of the critical extended phases give an interesting result. When incommensurate hopping modulation is turned on we see a "smeared mobility edge"

*m.yahyavi@bilkent.edu.tr

†hetenyi@fen.bilkent.edu.tr; hetenyi@phy.bme.hu

‡tanatar@fen.bilkent.edu.tr

phase, in which the rise in the MIPR between the localized and extended regions is gradual, rather than sharp (Fig. 7). Other GAAHs all show a sharp jump [22,25] in mobility edge phases. When, in addition, incommensurate on-site potential modulation is turned on, the rise in MIPR between localized and extended regions are sharp again, but there are more than one such jumps in MIPR. In these last two incommensurate studies topological edge states exist in all phases. Also, for the commensurate lattice, we investigate the Chern numbers of the main gaps during the change of the modulated p-wave SC pairing strength. We find that values of the Chern numbers are changing with and without on-site potential when we tune the modulated p-wave SC pairing strength. The modulated p-wave pairing strength changes; the energy spectrum alters from the triangular lattice like Hofstadter butterfly to one which is square lattice like.

Our paper is organized as follows. In the next section (Sec. II), the generalized version of the GAAH model that includes nearest-neighbor and next-nearest-neighbor p-wave SC pairing is defined on the infinite lattice. In Sec. III, we extend the 1D model to an "ancestor" 2D p-wave SC model. In Sec. IV, we check topological properties of the pure commensurate lattice for the $\beta = 1/2$. In Sec. V, we consider the incommensurate modulations case for β, where we will discuss the metal-insulator transition, and especially the influences of the modulated p-wave SC pairing strength on this transition. In Sec. VI, for pure commensurate lattice, the corresponding Hofstadter butterflies are discussed in detail. We conclude the paper in Sec. VII.

II. MODEL

The generalized one-dimensional Aubry-André-Harper model with p-wave SC pairing which we study here is described by the following Hamiltonian:

$$\hat{H} = -\sum_j [(t+\tau_j)c_j^\dagger c_{j+1} + \text{H.c.}] + \sum_j (\Delta+\delta_j)c_j^\dagger c_{j+1}^\dagger + \text{H.c.} + \sum_j V_j \hat{n}_j, \quad (1)$$

where

$$\begin{aligned} \tau_j &= \tau\ \cos(2\pi\beta j + \phi_\tau), \\ \delta_j &= \delta\ \cos(2\pi\gamma j + \phi_\delta), \\ V_j &= V\ \cos(2\pi\beta j + \phi_V). \end{aligned} \quad (2)$$

Here τ_j is commensurate (incommensurate) hopping modulations with periodicity $1/\beta$ and phase factor ϕ_τ and V_j is the diagonal Aubry-André potential with periodicity $1/\beta$ and phase factor ϕ_V, respectively. The corresponding hopping modulation amplitude is set by τ and V is the on-site potential strength. $\hat{n}_j = c_j^\dagger c_j$ are number operators, $c_j^\dagger(c_j)$ are creation (annihilation operators) at position j on the lattice, and t is the hopping (or tunneling) amplitudes to the nearest neighbors and set to be the unit of the energy ($t = 1$). Also, δ_j is a SC modulation with periodicity $1/\beta$ and phase factor ϕ_δ. Here δ and Δ are the strengths of the SC pairing gap taken to be real.

In the limit $\Delta = \delta = 0$, this model reduces to the generalized Aubry-André-Harper model introduced by Ganeshan *et al.* [26]. If $\delta = 0$ and $\phi_\tau = \phi_V$, this model reduces to the GAAH model with p-wave SC pairing introduced in Ref. [19] and studied in Ref. [23]. If we set $\tau = \delta = 0$ the model exhibits an Anderson localization transition when $V > 2(t+\Delta)$ [31]. On the other hand, if Δ and δ are zero, but τ and V are finite, and when the relation between the hopping modulation and on-site phases are fixed, for example, $\phi_V = \phi_\tau + \beta\pi$, the GAA model can be formally derived from an ancestor 2D quantum Hall system on a lattice (Hofstadter model) with diagonal (next-nearest-neighbor) hopping terms [13,32,33]. Here we keep our notations general with $\phi_\tau = \phi_\delta = k_y$ and $\phi_V = k_y + \varphi$ as independent variables. The off-diagonal modulation has an additional phase φ.

III. 2D ANALOG OF THE GENERALIZED AUBRY-ANDRÉ MODEL WITH p-WAVE SUPERCONDUCTIVITY

The Hamiltonian of the 1D GAAH model with p-wave superfluid pairing we consider in this paper can be made to correspond to a 2D p-wave SC model. For any given k_y, the GAAH model of Eq. (1) can be viewed as the k_yth Fourier component of a general 2D Hamiltonian. On the other hand, k_y is the second degree of freedom; hence we define the operator c_{n,k_y} that satisfies the following commutation relation:

$$\{c_{n,k_y}, c_{\acute{n},\acute{k}_y}^\dagger\} = \delta_{n,\acute{n}}\delta_{k_y,\acute{k}_y}. \quad (3)$$

Therefore, the 2D Hamiltonian can be expressed in terms of $\hat{H}$ as

$$\hat{\mathcal{H}} = \frac{1}{2\pi}\int_0^{2\pi} \hat{H}(k_y)dk_y, \quad (4)$$

where in the Hamiltonian of Eq. (1), we replaced the operators c_n with c_{n,k_y}. The corresponding Hamiltonian can be written as

$$\begin{aligned} \hat{H}(k_y) = &-\sum_n \left[(t+\tau_n)c_{n,k_y}^\dagger c_{n+1,k_y} + \text{H.c.}\right] \\ &+ \sum_n \left[(\Delta+\delta_n)c_{n,k_y}^\dagger c_{n+1,-k_y}^\dagger + \text{H.c.}\right] \\ &+ \sum_n V_n c_{n,k_y}^\dagger c_{n,k_y}. \end{aligned} \quad (5)$$

Fourier transforming only in the y direction

$$c_{n,k_y} = \sum_m e^{-ik_y m} c_{n,m} \quad (6)$$

allows us to easily calculate the 2D Hamiltonian as

$$\begin{aligned} \hat{\mathcal{H}} = \sum_{n,m} -\Big\{ & t c_{n,m}^\dagger c_{n+1,m} \\ & - \left[\frac{\tau}{2}(e^{i2\pi\beta n} c_{n,m}^\dagger c_{n+1,m+1} + e^{-i2\pi\beta n} c_{n,m}^\dagger c_{n+1,m-1})\right] \\ & + \left[\frac{\delta}{2}(e^{i2\pi\beta n} c_{n,m}^\dagger c_{n+1,m+1}^\dagger + e^{-i2\pi\beta n} c_{n,m}^\dagger c_{n+1,m-1}^\dagger) \right. \\ & \left. + \Delta c_{n,m} c_{n+1,m}\right] + \frac{V}{2} e^{i(2\pi\beta n+\varphi)} c_{n,m}^\dagger c_{n,m+1} + \text{H.c.}\Big\}. \end{aligned} \quad (7)$$

When $\varphi = 0$, the 2D system has isotropic next-nearest-neighbor hoppings and the corresponding 1D Hamiltonian has

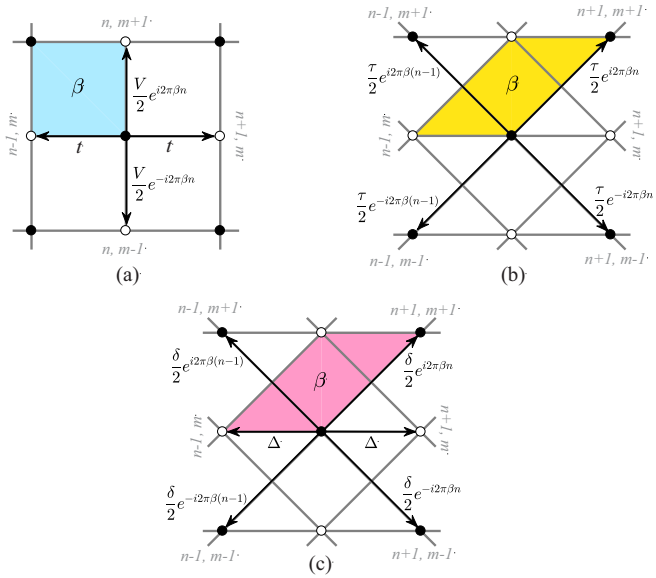

FIG. 1. Graphical presentations of extended 1D GAAH with nearest and next-nearest hopping (SC pairing) and on-site potential to a 2D Hamiltonian. In the presence of a perpendicular magnetic field with β flux quanta per unit cell, the electrons hop on a rectangular lattice. (a) This is the 2D "ancestor" of the diagonal GAAH model which the hopping is to nearest neighbors, (b) this is the 2D ancestor of the off-diagonal GAAH model which the hopping is to next-nearest neighbors, and (c) this is the 2D ancestor of the SC pairing of GAAH model which the hopping is to nearest and next-nearest neighbors. Each rectangular plaquette shown in a different color is pierced by β flux quanta.

the same phase k_y in the off-diagonal and diagonal modulations. This Hamiltonian describes a 2D lattice in the presence of a uniform perpendicular magnetic field with β flux quanta per unit cell as shown in Fig. 1.

IV. COMMENSURATE MODULATION: THE CASE OF $\beta = \frac{1}{2}$

Setting $\beta = \frac{1}{2}$ in Eq. (1), and all three phases to zero, the lattice becomes bipartite. Introducing the notation c_i and d_i for the two sublattices and Fourier transforming using the Nambu basis $c_k^\dagger, d_k^\dagger, c_{-k}, d_{-k}$, the Hamiltonian becomes

$$\hat{H} = -2t\,\cos(k)\sigma_z \otimes \sigma_x - 2\tau\,\sin(k)\sigma_z \otimes \sigma_y + V\sigma_z \otimes \sigma_z - 2\Delta\,\sin(k)\sigma_y \otimes \sigma_x + 2\delta\,\cos(k)\sigma_y \otimes \sigma_y. \tag{8}$$

Note that the first three terms correspond to $\sigma_z \otimes \hat{H}_{RM}$, where $\hat{H}_{RM}$ is the Rice-Mele Hamiltonian. It follows that if we set $\Delta = \delta = V = 0$ the model consists of two independent SSH models (which are topological), and it is possible to define an adiabatic process in which charge is pumped across the unit cell (the topological edge states support charges localized at the edges of the system). In a similar vein, keeping $V = 0$, it is possible to pair the two $\cos(k)$ with the two $\sin(k)$ terms in four ways. Keeping the other parameters zero leads to other possible topological states, or possible adiabatic pumping processes. Of the remaining three, two are Majorana fermions and the fourth one a Cooper pair. For example, we can take $\tau = \delta = 0$ resulting in

$$\hat{H} = [-2t\,\cos(k)\sigma_z - 2\Delta\,\sin(k)\sigma_y] \otimes \sigma_x. \tag{9}$$

In other words, a 2×2 Hamiltonian of the SSH form, but the adiabatic pumping in this case would not correspond to a charge pump, because different members of the Nambu bases are coupled by the matrix elements. For each of the four cases it is possible to construct the time-reversal, particle-hole symmetry operators, as well as the chiral symmetry operators using the "left" or the "right" part of the direct product and multiplying with an identity operator from the other side. They all fall in the BDI symmetry class [34].

V. INCOMMENSURATE MODULATION

When β is irrational, the lattice is incommensurate. We choose $\beta = (\sqrt{5}-1)/2$, the golden ratio, but all the conclusions can also be generalized to other incommensurate situations. In this paper, for the incommensurate modulation case, we shall study the interplay of the SC modulation pairing δ with the incommensurate hopping amplitude and potential, respectively, and then we determine the phase diagram of the model. The Hamiltonian can be diagonalized by the Bogoliubov–de Gennes (BdG) transformation [35,36]

$$\eta_n^\dagger = \sum_{j=1}^{L} [u_{n,j} c_j^\dagger + v_{n,j} c_j], \tag{10}$$

where $n = 1, \ldots, L$, is the energy band index and $u_{n,j}$ and $v_{n,j}$ denote the two wave function components at the site j assumed to be real. On this basis the wave function of the Hamiltonian becomes

$$|\Psi_n\rangle = \eta_n^\dagger |0\rangle = \sum_{j=1}^{L} [u_{n,j} c_j^\dagger + v_{n,j} c_j] |0\rangle. \tag{11}$$

Then the Hamiltonian in Eq. (1) can be diagonalized in terms of the operators η_n and $\eta_n^\dagger$ as

$$\hat{H} = \sum_{n=1}^{L} \varepsilon_n \left(\eta_n^\dagger \eta_n - \frac{1}{2} \right), \tag{12}$$

with ε_n being the spectrum of the quasiparticles. The Schrödinger equation $H|\Psi_n\rangle = \varepsilon_n |\Psi_n\rangle$ can be written as

$$\begin{aligned} &-(t+\tau_{j-1})u_{n,j-1} + (\Delta+\delta_{j-1})v_{n,j-1} + V_j u_{n,j} \\ &\quad - (t+\tau_j)u_{n,j+1} - (\Delta+\delta_j)v_{n,j+1} = \varepsilon_n u_{n,j}, \\ &(t+\tau_{j-1})v_{n,j-1} - (\Delta+\delta_{j-1})u_{n,j-1} - V_j v_{n,j} \\ &\quad + (t+\tau_j)v_{n,j+1} + (\Delta+\delta_j)u_{n,j+1} = \varepsilon_n v_{n,j}. \end{aligned} \tag{13}$$

Representing the wave function as

$$|\Psi_n\rangle = [u_{n,1}, v_{n,1}, u_{n,2}, v_{n,2}, \ldots, u_{n,L}, v_{n,L}]^T, \tag{14}$$

the Hamiltonian H can be written as a $2L \times 2L$ matrix,

$$H_n = \begin{pmatrix} A_1 & B & 0 & \cdots & \cdots & \cdots & C \\ B^\dagger & A_2 & B & 0 & \cdots & \cdots & 0 \\ 0 & B^\dagger & A_3 & B & \cdots & \cdots & 0 \\ \vdots & \ddots & \ddots & \ddots & \ddots & \ddots & \vdots \\ 0 & \cdots & 0 & B^\dagger & A_{L-2} & B & 0 \\ 0 & \cdots & \cdots & 0 & B^\dagger & A_{L-1} & B \\ C^\dagger & \cdots & \cdots & \cdots & 0 & B^\dagger & A_L \end{pmatrix}, \quad (15)$$

where

$$A_j = \begin{pmatrix} V_j & 0 \\ 0 & -V_j \end{pmatrix}, \quad (16)$$

$$B = \begin{pmatrix} -(t+\tau_j) & -(\Delta+\delta_j) \\ \Delta+\delta_j & t+\tau_j \end{pmatrix}, \quad (17)$$

and

$$C = \begin{pmatrix} -(t+\tau_{j+1}) & \Delta+\delta_{j+1} \\ -(\Delta+\delta_{j+1}) & t+\tau_{j+1} \end{pmatrix}, \quad (18)$$

for the lattice with periodic boundary conditions, or

$$C = \begin{pmatrix} 0 & 0 \\ 0 & 0 \end{pmatrix}, \quad (19)$$

for the lattice with open boundary conditions. Here we consider a chain of length L with periodic boundary conditions. The irrational β can be approximated by a sequence of rational numbers [37] [see Eq. (21)]. In our model we may expect the usual [12] delocalization transition that occurs in the original AA model in the incommensurate case. To show this, we calculate the mean inverse participation ratio (MIPR), which for a given normalized wave function $[\sum_{j=1}^{N}(u_{n,j}^2 + v_{n,j}^2) = 1]$ is defined as [38,39]

$$\text{MIPR} = \frac{1}{2N}\sum_{n=1}^{2N}\sum_{j=1}^{N}\left(u_{n,j}^4 + v_{n,j}^4\right), \quad (20)$$

where n is the index of energy levels and $u_{n,j}$ and $v_{n,j}$ are the solution to the BdG equations. It is well known that, for an extended state, MIPR $\to \frac{1}{L}$ and the MIPR tends to zero in the thermodynamic limit (for large L); however, MIPR tends to a finite value for a localized state even in the thermodynamic limit. In the following, we will calculate the MIPR for different configurations of our GAAH model with p-wave pairing for generic and off-diagonal cases to characterize the phase boundaries separating localized, critical, and extended phases.

Next, in order to clarify the nature of different phases in our model, we perform multifractal analysis [32] of the eigenfunctions, a technique which was applied to study the quasiperiodic chain with p-wave pairing [23] and also the original Aubry-André model [32,40]. From the above assumption regarding the irrational value of β, the golden ratio can be approached by the Fibonacci numbers via the relation

$$\beta = \lim_{m\to\infty}\frac{F_{m-1}}{F_m}, \quad (21)$$

where F_m is the mth Fibonacci number. We choose the chain $L = F_m$. It is recursively defined by the relation $F_{m+1} = F_m + F_{m-1}$, with $F_0 = F_1 = 1$. The probability measure can be defined from a wave function of Eq. (11) as

$$p_{n,j} = u_{n,j}^2 + v_{n,j}^2, \quad (22)$$

which is normalized ($\sum_{j=1}^{F_m} p_{n,j} = 1$). The scaling index $\gamma_{n,j}$ for $p_{n,j}$ is defined by

$$p_{n,j} \sim F_m^{-\gamma_{n,j}}. \quad (23)$$

In the scaling limit $m \to \infty$, according to the multifractal theorem [40], the number of sites which have a scaling index between γ and $\gamma + d\gamma$ is proportional to $F_m^{f(\gamma)}$. To distinguish the extended, critical, and localized wave functions, only a part of $f(\gamma)$ is required. For the extended wave functions, the maximum probability measure scales as $\max[p_{n,j}] \sim F_m^{-1}$; thus we have $\gamma_{\min} = 1$. For a localized wave function, $p_{n,j}$ is finite ($\gamma = 0$, $[f(0) = 0]$) at some sites but on other sites it is exponentially small ($\gamma = \infty$, $[f(\infty) = 1]$); thus we have $\max[p_{n,j}] \sim F_m^0$, or $\gamma_{\min} = 0$. On the other hand, for the critical wave functions, on a finite interval $[\gamma_{\min}, \gamma_{\max}]$, $f(\gamma)$ is a smooth function with $0 < \gamma_{\min} < 1$. Therefore, for distinguishing the extended, critical, and localized wave functions, we need to calculate $\gamma_{\min}$ which is defined as $\max[p_{n,j}] \sim F_m^{-\gamma_{\min}}$. Namely,

$$\begin{aligned} &\gamma_{\min} = 1, \quad \text{for an extended wave function,} \\ &\gamma_{\min} \neq 0, 1, \quad \text{for a critical wave function,} \\ &\gamma_{\min} = 0, \quad \text{for a localized wave function.} \end{aligned} \quad (24)$$

Note that, here in our calculation, we plotted the average of $\gamma_{\min}$ over all the eigenstates ($\overline{\gamma}_{\min}$), which can be written as

$$\overline{\gamma}_{\min} = \frac{1}{2F_m}\sum_{n=1}^{2F_m}\gamma_{\min}^n. \quad (25)$$

A. Off-diagonal GAAH model with p-wave pairing

The case $V = 0$ corresponds to the off-diagonal GAAH model with p-wave pairing. We calculate the phase diagram as a function of the modulation strength of incommensurate p-wave pairing (δ) and the modulation strength of incommensurate hopping (τ), focusing mostly on the case $k_y = \pi/2$. We choose $\varphi = \beta\pi$. This off-diagonal GAAH model in the limit $\Delta = 0$ and $\delta = 0$ exhibits nontrivial zero-energy edge modes [24,26] and in a large parameter space preserves the critical states [25]. We find that the topological properties and localization of this system are profoundly affected by a finite δ. The main new feature compared to Ref. [25] is various phases with mobility edges. The phase diagram based on the MIPR of the off-diagonal GAAH model with p-wave pairing (without hopping modulations and site-diagonal potential) is shown in Fig. 2. The extended phase (regions I and II), the mobility-edge phase (region III), and critical phase (region IV) are separated by the black solid lines. Regions I, II, and III host two zero-energy modes as a result of nontrivial topology which only appear for open boundary conditions. In Fig. 3, we show the distribution of the inverse participation ratio (IPR) for different eigenstates. In regions I [Fig. 3(a)], II [Fig. 3(b)], and III [Fig. 3(c)], respectively, we find the zero-energy topological edge modes (large red dots) indicating the topologically nontrivial phase. For almost all eigenstates, the

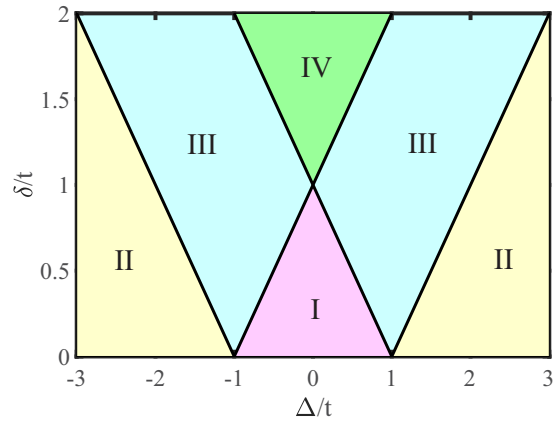

FIG. 2. Phase diagram of the off-diagonal GAAH model as a function of the p-wave incommensurate modulation amplitude δ and the p-wave pairing strength Δ. The hopping incommensurate modulation amplitude is set to $\tau = 0$ and the phase in the incommensurate modulation is set to $k_y = \pi/2$ and $\varphi = \beta\pi$. The phases are (I and II) extended phases, (III) topological critical phase, and (IV) nontopological critical phase.

IPR distribution has the same characteristics (around 10^{-4}) in regions I and II, which shows that all the eigenstates are extended. In regions III and IV, the value of IPR is around 10^{-2}, which is two orders of magnitude larger than in the extended phase. These dispersed distributions suggest that these regions (III and IV) are critical phases. These results confirm that regions I, II, and III are in the nontrivial-topological phases, while the region IV is trivial phase. Also, as shown in Fig. 4, region IV is topologically trivial and the edge modes (indicated in red color in the figure), in the regions I and III are found to be very robust. For comparison, in Ref. [24] the robustness of edge states against modulations of various types was analyzed. It was argued that a diagonal potential displaces edge states from zero energy. In our case the edge states occur in the case of off-diagonal disorder when $\tau = 0$ and survive

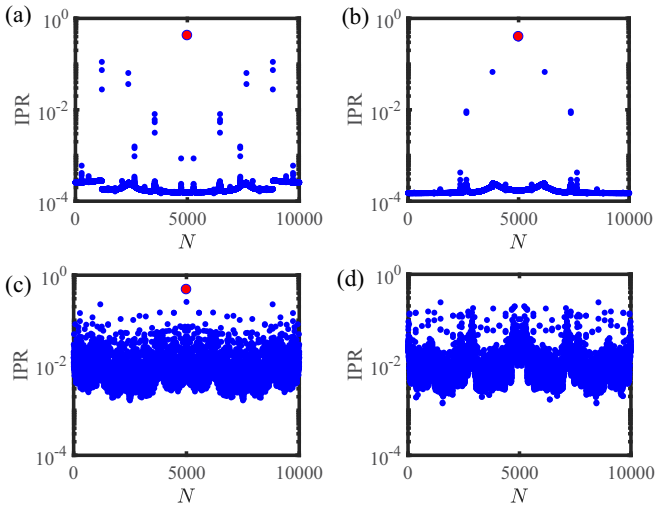

FIG. 3. Distribution of IPRs over all the eigenstates for (a) and (b) extended phases, (c) topological critical phase, and (d) nontopological critical phase of Fig. 2.

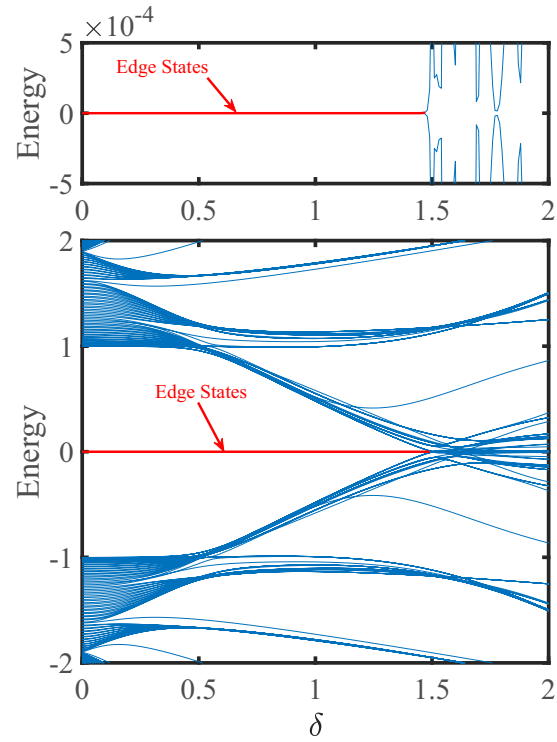

FIG. 4. Energy spectrum of the off-diagonal GAAH model with p-wave pairing plotted as a function of δ under OBCs with $L = 100$ lattice sites. The model parameters are $\tau = 0$, $V = 0$, and $\Delta = 0.5$. Inside the regions I and II (see Fig. 2) there are edge states.

even after a finite diagonal potential is turned on and the model undergoes Anderson-like localization (see Sec. IV B).

The evolution of the MIPR on a logarithmic scale at three values of $\delta = 0.5$, 1, and 1.5 is shown in Fig. 5. We find that the MIPR changes abruptly from one phase to another as a function of Δ and δ. There are four turning points and the change of MIPR at these points becomes sharper with increasing system size L (results not shown). Thus, in the thermodynamic limit $L \to \infty$, a discontinuity at the turning

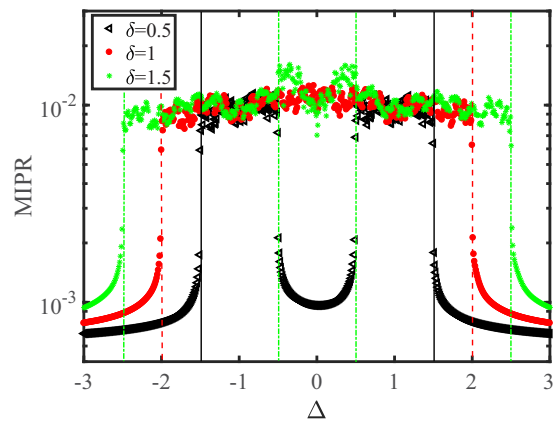

FIG. 5. MIPR as a function of p-wave superfluid pairing Δ for the indicated values of modulation amplitude δ. The dashed lines, dot-dashed lines, and solid lines demonstrate the abrupt changes of the MIPR at phase boundaries.

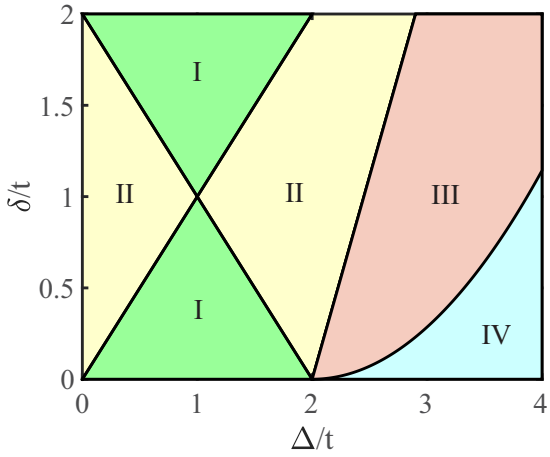

FIG. 6. Phase diagram of the off-diagonal GAAH model with the p-wave incommensurate modulation amplitude $0 < \delta \leqslant 2$ and the p-wave pairing strength $0 \leqslant \Delta \leqslant 4$. The hopping incommensurate modulation amplitude is set to $\tau = 1$ and the phase in the incommensurate modulation is set to $k_y = \pi/2$ and $\varphi = \beta\pi$. The phases are (I) localized phase, (II) critical localized phase, (III) critical extended phase, and (IV) extended phase.

points signals the phase transitions among the mobility-edge, the extended, and the critical phases. We have also considered the dependence of the phase diagram on nonzero τ. By calculating the MIPR, we find that the localization properties of this model are significantly affected by turning on the off-diagonal hopping modulation of τ. For $\tau = 1$, the results are summarized in the phase diagram shown in Fig. 6. There are four distinct phases, localized phase (I), critical localized phase (II), critical extended phase (III), and extended phase (IV), separated by solid black lines. In Fig. 7, we show examples of the distribution of IPR over different eigenstates for localized phase (I), critical localized phase (II), critical extended phase (III), and extended phase (IV)

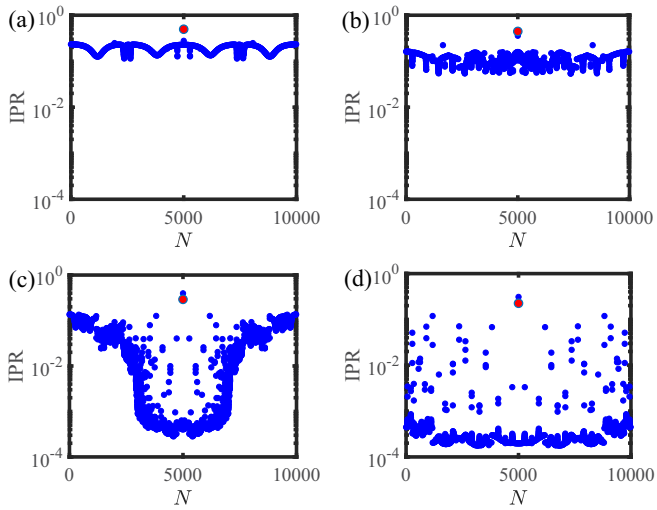

FIG. 7. Distribution of IPRs over all the eigenstates for region (a) I (localized phase), (b) II (critical localized phase), (c) III (critical extended phase), and (d) IV (extended phase) of Fig. 6.

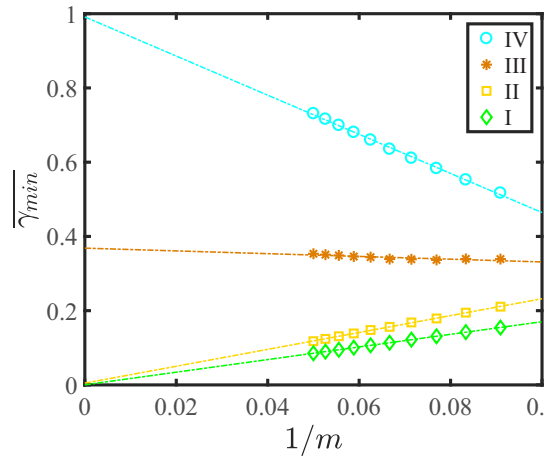

FIG. 8. $\overline{\gamma_{\min}}$ as function of $1/m$ for regions I (localized phase), II (critical localized phase), III (critical extended phase), and IV (extended phase) of Fig. 6.

of Fig. 6. Topological edge states are found in all phases. An interesting situation is depicted in Fig. 7(c): The MIPR indicates the simultaneous presence of localized and extended states, as in a mobility edge phase, but here the boundary is smeared between the two. As the eigenenergy increases in Fig. 7(c), the IPR smoothly changes from a typical value for the localized states around 10^{-1} to a typical value for the extended states 10^{-4}. The smooth changes of the IPR suggest that there exist the semimobility edge in the energy spectrum. Also, for these selected phases in Fig. 8, we plotted $\overline{\gamma}_{\min}$ as a function of $1/m$. For the localized phase and the critical localized phase $\overline{\gamma}_{\min}$ extrapolates to zero, while for the critical extended phase $\overline{\gamma}_{\min}$ extrapolates to 0.38, and for the extended phase $\overline{\gamma}_{\min}$ extrapolates to 1. These results also confirm our phase diagram in Fig. 6.

Figure 9 shows the MIPR of the model as a function of Δ with $\tau = 1$ and $\delta = 0.5$ for different system sizes. We have checked that, with increasing L, the system is in the localized region (I) for $\delta - \tau + 1 < \Delta < \tau - \delta + 1$. Also, for the extended phase (III) the MIPR is finite and depends on the system size (L). In this phase, the MIPR satisfies the finite size scaling (FSS) form, $\text{MIPR} = bL^{-\eta}$. At the $\Delta/t = 3.5$, $\eta = 0.63$. For this phase, with the increase L, MIPR tends to zero. The MIPR among localized, critically localized, critical extended, and extended phases satisfies

$$\text{MIPR}_E < \text{MIPR}_{CE} < \text{MIPR}_{CL} < \text{MIPR}_L. \quad (26)$$

We verified this expression by checking the FSS in the whole phase diagram (results not shown).

B. Generic GAAH model with p-wave pairing

We also investigate the generic p-wave pairing GAAH model with modulated on-site potentials, modulated off-diagonal hopping terms, and modulated p-wave pairing terms. In this section, we explore the influence of the modulated on-site potential on the phase transition. It is clear that varying V changes the phase diagram. So, due to the modulation in the p-wave pairing term, we find that the system has a stronger tendency to become extended as a function of Δ/t when the

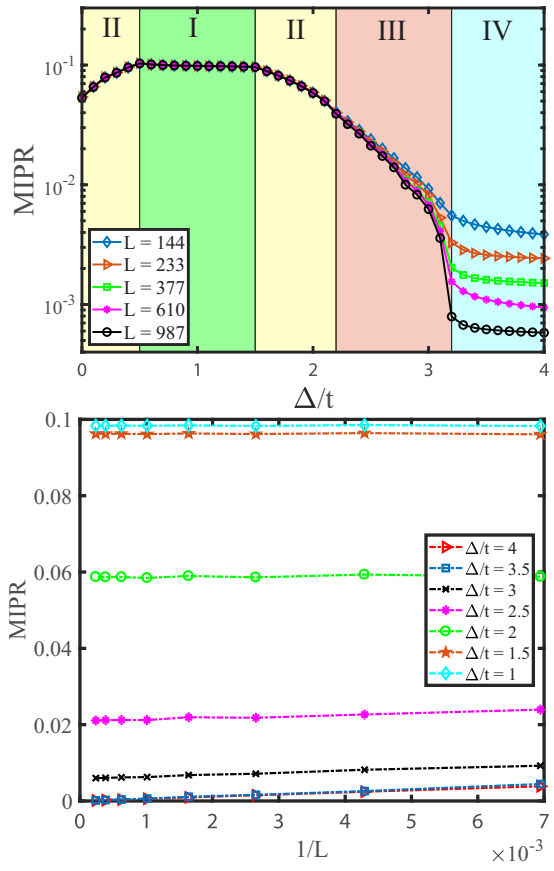

FIG. 9. Upper panel: MIPR (log scale) as a function of p-wave superfluid pairing Δ/t for different chain lengths L for $\tau = 1$ and $\delta = 0.5$. Bottom panel: MIPR with the inverse system size $1/L$. For the extended phase, MIPR tends to zero as L increases.

disordered on-site potential (V) is varied. In Fig. 10, the phase diagram of the generic GAAH model for the case $V/t = 1$ is shown. The phase boundary separating the localized phase, critical localized phase, critical extended phases, and extended phases vary rapidly with the SC pairing. We also performed a FSS analysis for this phase diagram (results not shown). When $V/t = 1$, it is clear that for $\delta/t < 1$, the localized phase disappears and the critical localized phase increases sharply. We also focus on the distribution of IPR with different eigenstates and multifractal analysis [32] for this case. An example of determining $\overline{\gamma}_{\min}$ as a function of $1/m$ in phases I, II, III, and IV of Fig. 10 is shown in Fig. 11. For this phase diagram, $\overline{\gamma}_{\min}$ extrapolates to zero if we are in I phase (in this case, the multifractal analysis of the wave function shows that all wave functions are in localized states) and to 1 if are in IV phase (in this case, the multifractal analysis of wave function shows that all of the wave functions are in extended state). The distribution of IPR in the eigenstates, shown in Fig. 12, indicates that almost all the eigenstates IPR are close to each other in phase I (being around 10^{-1}) and phase IV (being around 10^{-4}). For phases II and III, the multifractal analysis of wave function is shown in Figs. 11(b) and 11(c). For the critical localized phase (II), $\overline{\gamma}_{\min}$ extrapolates to 0.245 and, for the critical extended phase (III), $\overline{\gamma}_{\min}$ extrapolates to 0.685. Again, as in Fig. 8, all phases exhibit topological

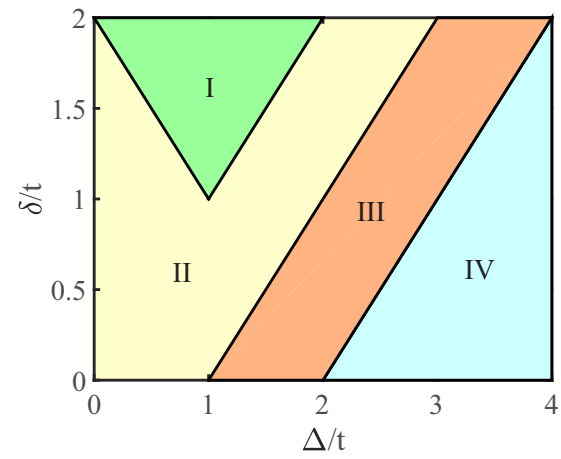

FIG. 10. Phase diagram of the generic GAAH model with the p-wave incommensurate modulation amplitude $0 < \delta \leqslant 2$ and the p-wave pairing strength $0 \leqslant \Delta \leqslant 4$. The hopping incommensurate modulation amplitude is set to $\tau = 1$, the on-site potential incommensurate modulation amplitude is set to $V/t = 1$, and the phase in the incommensurate modulation is set to $k_y = \pi/2$ and $\varphi = \beta\pi$. The phases are (I) localized phase, (II) critical localized phase, (III) critical extended phases, and (IV) extended phases.

edge modes. As the eigenenergy increases in Fig. 12(b) for the critical localized state, the IPR suddenly jumps from a typical value for the localized states around 10^{-1} to a typical value for the extended states 10^{-4}, but for the critical extended state this happens twice [see Fig. 12(c)]. Models of which we are aware [22,25] show one mobility edge jump. Recall that in Fig. 8 it was also the critical extended state which showed unusual behavior—the smeared mobility edge.

In summary, we find that due to the modulation in the SC pairing the incommensurate generic GAAH model with p-wave pairing delocalizes easier when varying the disordered on-site potential, when $\delta < V$. We find that the topological properties of the generic GAAH model with p-wave pairing

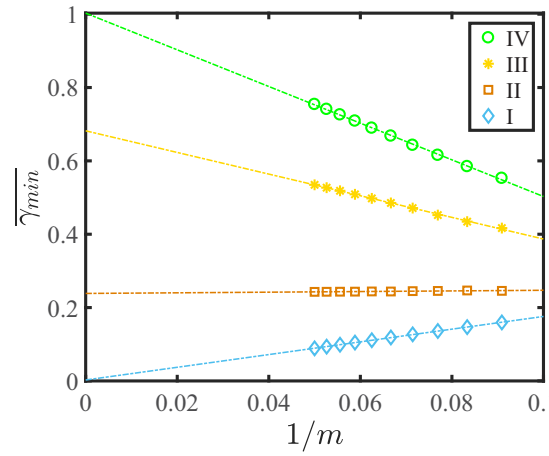

FIG. 11. $\overline{\gamma_{\min}}$ as function of $1/m$ for regions I (localized phase), II (critical localized phase), III (critical extended phase), and IV (extended phase) of Fig. 10.

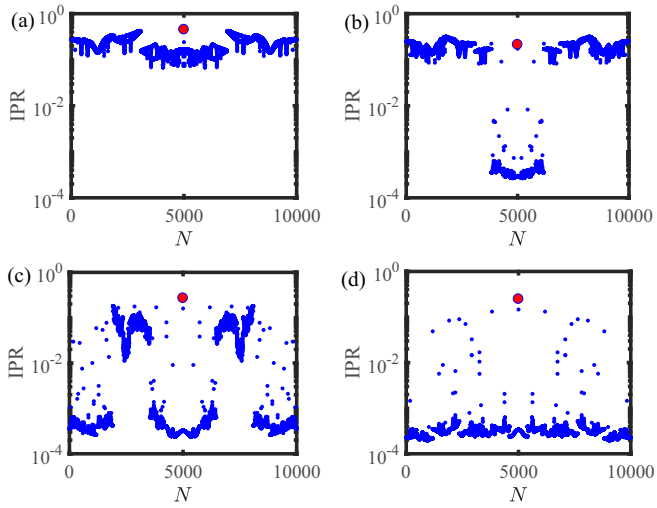

FIG. 12. Distribution of IPRs over all the eigenstates for (a) regions I (localized phase), (b) II (critical localized phase), (c) III (critical extended phase), and (d) IV (extended phase) of Fig. 10.

are significantly affected by turning on the modulated on-site potential and modulated p-wave SC pairing.

VI. COMMENSURATE MODULATION

When β is rational, the lattice is commensurate. It is known that in the commensurate case [19], the system will not undergo a localization-delocalization transition as in the incommensurate case. When $\beta = 1/2$, both Kitaev-like and Su-Schrieffer-Heeger–like (SSH-like) models are included in this GAAH model with p-wave SC pairing for commensurate modulations. The Hamiltonian of Eq. (1) is reduced to the SSH model for $V = \Delta = \delta = 0$ and to the Kitaev model for $\tau = \delta = 0$. In order to determine the different phase boundaries and characterize the topological phases, we need to calculate the effect of modulated SC pairing on the topological properties of the system. In the following, we characterize the topological nature of the modulated SC pairing by calculating the evolution of Chern numbers [41] for the major gaps of the spectrum.

Chern numbers

Chern numbers can be calculated from the density with respect to changes in the magnetic field using the Středa formula [42,43]. In lattice systems, the Chern number can be written as

$$C = \frac{\partial \bar{n}(\beta)}{\partial \beta}, \tag{27}$$

where $\bar{n}$ is the number of levels below the Fermi level. This formula is valid when the chemical potential lies in a gap [42]. Formally, the evaluation of the Chern numbers can be calculated by k-space integration of the Berry curvature over the Brillouin zone. In Fig. 13 we present the Hofstadter butterfly for the case $V/t = 0$, $\lambda = 0.3$, $\Delta = 0.4$, and various values of δ. The spectrum for $\delta = 0$ is clearly formed by two triangular-lattice Hofstadter butterflies separated by a large gap. The Hofstadter butterfly separation is controlled by the

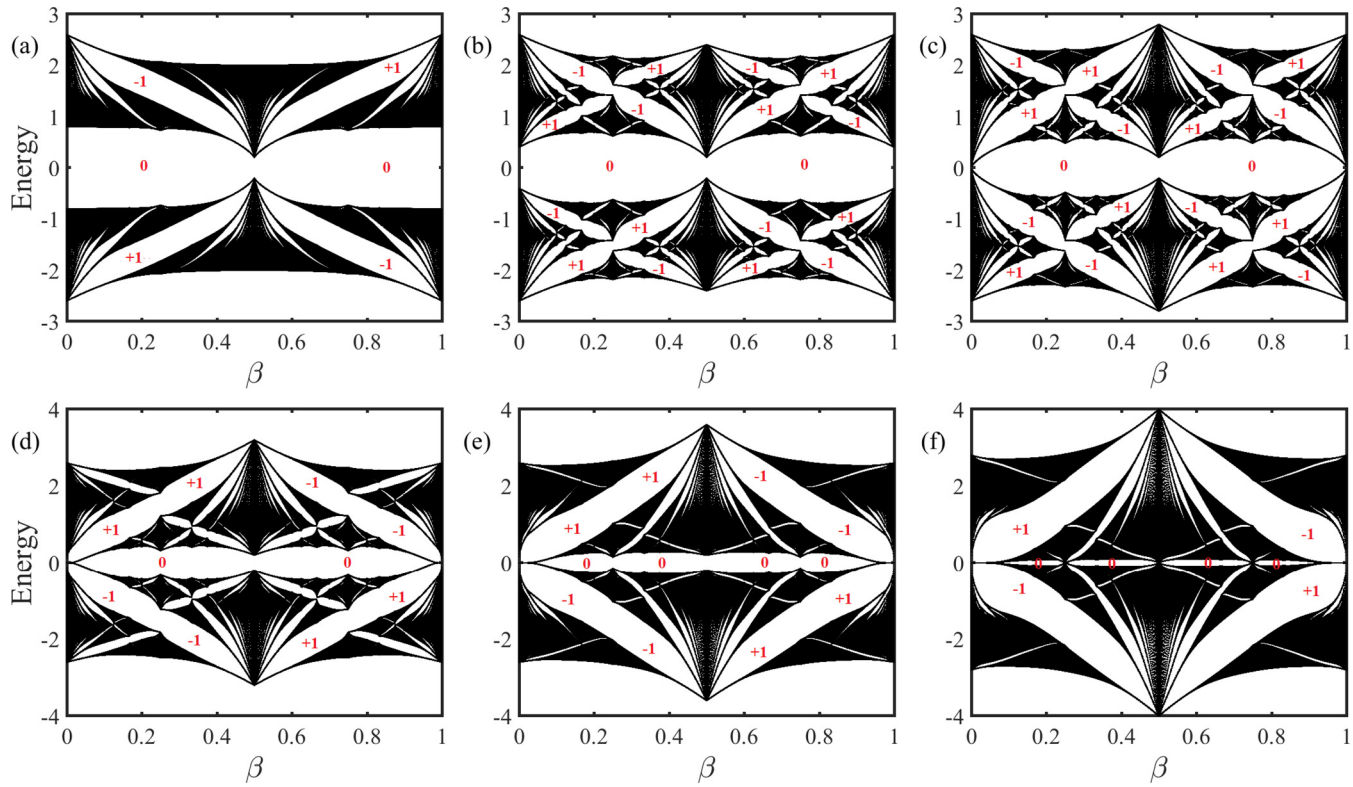

FIG. 13. Hofstadter butterfly: Energy spectrum as a function of magnetic flux per plaquette β in Aubry-André lattice with $V = 0$, $\tau = 0.3$, $\Delta = 0.4$, and (a) $\delta = 0$, (b) $\delta = 0.2$, (c) $\delta = 0.4$, (d) $\delta = 0.6$, (e) $\delta = 0.8$, and (f) $\delta = 1$.

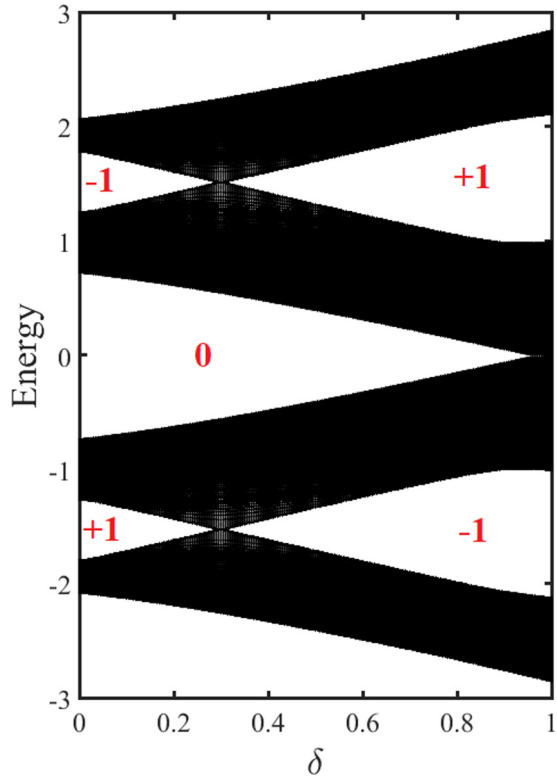

FIG. 14. Evolution of the energy bands for $\beta = 0.25$, $V = 0$, $\tau = 0.3$, and $\Delta = 0.4$ as function of δ shown in Fig. 13. Gaps are labeled with their Chern numbers.

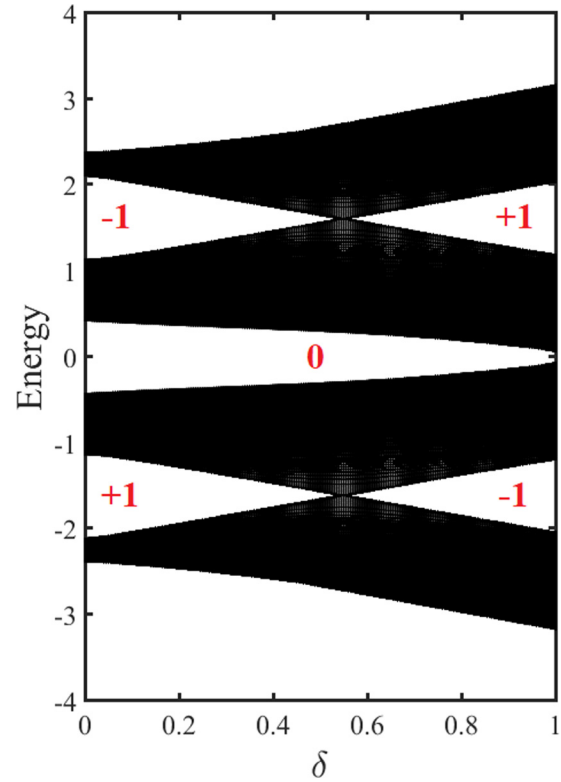

FIG. 16. Evolution of the energy bands for $\beta = 0.25$, $V = 1$, $\tau = 0.3$, and $\Delta = 0.4$ as function of δ shown in Fig. 15. Gaps are labeled with their Chern numbers.

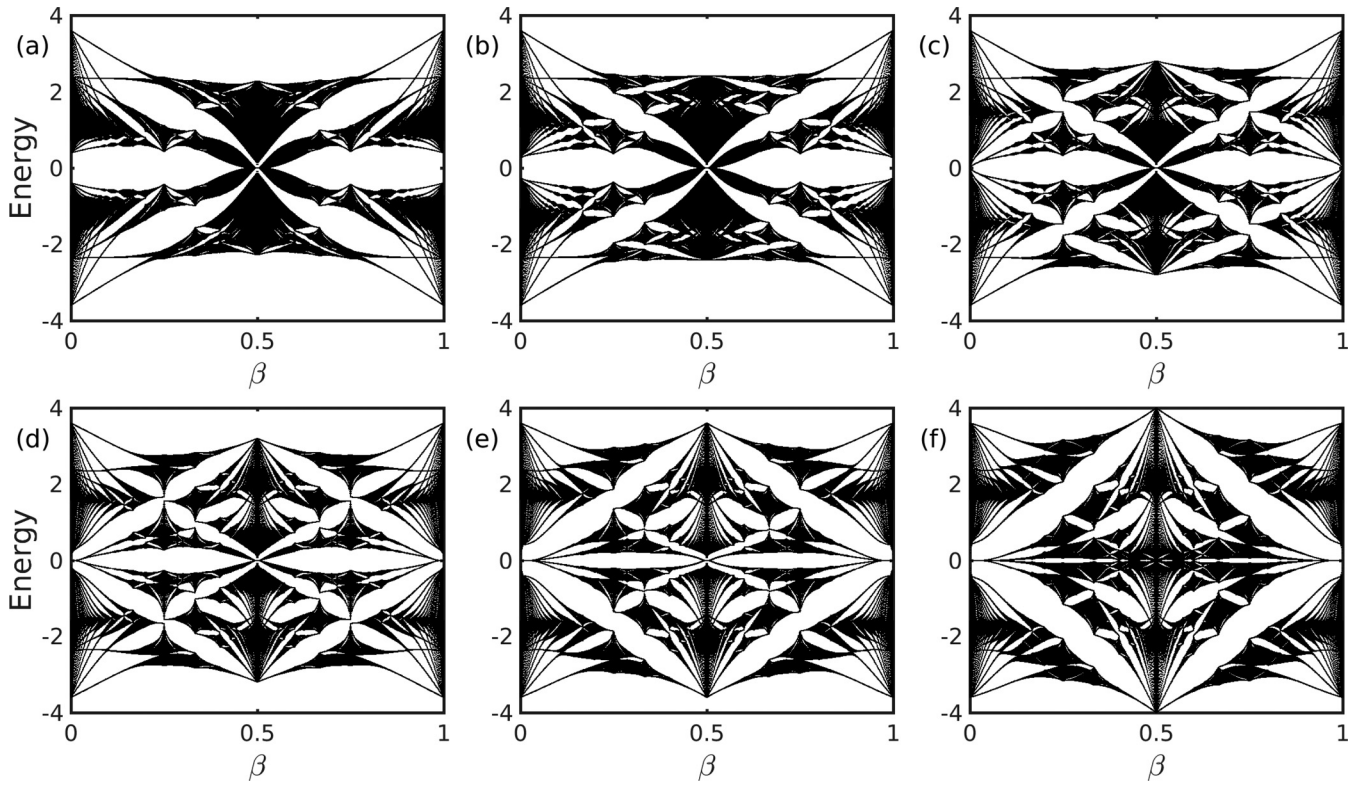

FIG. 15. Hofstadter butterfly: Energy spectrum as a function of magnetic flux per plaquette β in Aubry-André lattice with $V = 1$, $\tau = 0.3$, $\Delta = 0.4$, and (a) $\delta = 0$, (b) $\delta = 0.2$, (c) $\delta = 0.4$, (d) $\delta = 0.6$, (e) $\delta = 0.8$, and (f) $\delta = 1$.

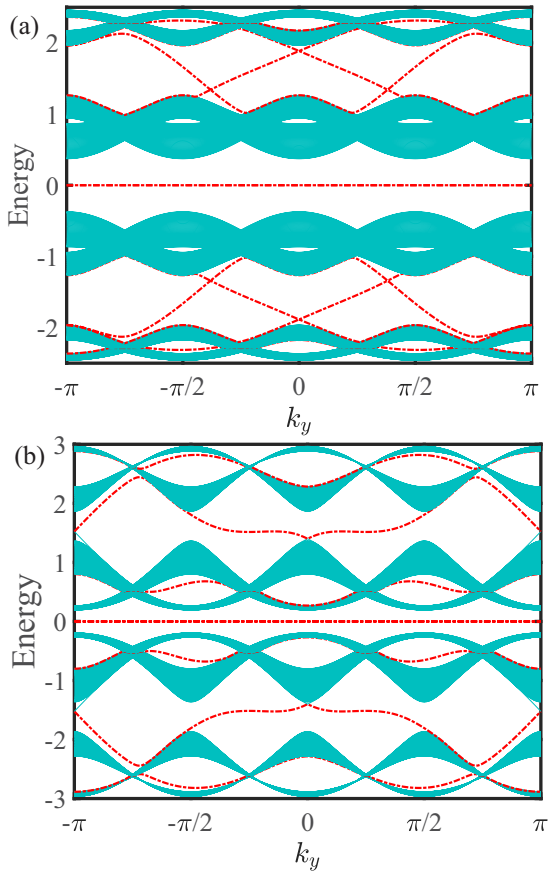

FIG. 17. Evolution of the energy bands for $\beta = 0.25$, $V = 1$, $\tau = 0.3$, and $\Delta = 0.4$ as function of δ shown in Fig. 15. Gaps are labeled with their Chern numbers.

SC parameter, δ (see Fig. 13). As illustrated in this figure, by changing δ, the upper (lower) butterfly approaches the square regime and then the honeycomb regime, which has different topology (in other words, at the $\beta = 0.2$ for upper lattice the Chern number changes from -1 to 1). Also, we see that, as δ is increased, the gaps at zero energy are sufficiently small and have not completely closed so that the overall butterfly shape is maintained. It is possible to understand this surprising result by considering the evolution of the energy bands at the points at which the main gap closes and reopens. For $V/t = 0$, $\lambda = 0.3$, $\Delta = 0.4$, and $\beta = 0.25$, these evolutions are demonstrated in Fig. 14. When the energy gap closes and reopens through this evolution, Chern numbers will change. For this case, we find two different regions corresponding to different Chern numbers, ± 1. An important observation is that the Chern number is sensitive to the δ parameter. As can be seen in Fig. 14, the whole area is covered by the triangular lattice, while the square lattice is confined to the point at gap closure, $\delta = 0.3$.

For the second case we consider $V \neq 0$, when the system has sublattice asymmetry. In this case, when $V \neq 0$ the evolution of the energy spectrum between the triangular lattice and the square lattice also occurs (see Fig. 15). The differences between the Hofstadter butterflies in the two sets of plots can be attributed to the spliting into two energy modes corresponding to two 1D Majorana chains coupled by the on-site potential, as discussed in Fig. 15. In Fig. 16, we show the evolution of bands as a function of δ. As a result of the on-site potential the critical δ_c increases. The Chern numbers associated with gaps are also indicated, which "switch" when the phase transition is encountered at quarter and three-quarters fillings. Figure 17 the band structure is shown as a function of k_y for two different values of δ. Topological edge states appear, in particular a zero energy edge state is present for the whole region in both cases.

VII. CONCLUSION

In this paper, we studied a GAAH model with modulated p-wave SC pairing, both in the commensurate and incommensurate cases. We mapped the derived 2D magnetic analog of the model, have shown that in the bipartite commensurate case four different topological excitations are possible, mapped the phase diagram of the model via studying the localization characteristics, and studied the evolution of its Hofstadter butterflies. The phase diagram is remarkably rich, exhibiting localized, extended, and critical phases, as well as topological edge states, which can occur in extended or critical cases. Several new phases were revealed, unique to the model with modulated p-wave pairing: In the critical extended phase when incommensurate p-wave pairing and hopping is turned on, the change in inverse participation ratios separating extended and localized regions is smeared, rather than sharp, as it happens [23] in the extended GAAH model without p-wave pairing modulation. When, in addition, the on-site potential is modulated the jumps between extended and localized regions are again sharp, but increase in number. For the commensurate case the modulated SC amplitude results in Hofstadter butterfly plots showing a transition from the rectangular to the square lattice as the parameter δ varies.

ACKNOWLEDGMENTS

B.H. was supported by the National Research, Development and Innovation Fund of Hungary within the Quantum Technology National Excellence Program (Project No. 2017-1.2.1-NKP-2017-00001). B.T. and M.Y. were supported by the Scientific and Technological Research Council of Turkey (TUBITAK) under Grant No. 117F125. B.T. is also supported by the Turkish Academy of Sciences (TUBA).

[1] P. W. Anderson, Phys. Rev. **109**, 1492 (1958).
[2] F. Evers and A. D. Mirlin, Rev. Mod. Phys. **80**, 1355 (2008).
[3] *50 Years of Anderson Localization*, edited by E. Abrahams (World Scientific, Singapore, 2010).
[4] H. Shima, T. Nomura, and T. Nakayama, Phys. Rev. B **70**, 075116 (2004).
[5] F. M. Izrailev, A. A. Krokhin, and N. M. Makarov, Phys. Rep. **512**, 125 (2012).

[6] J. Biddle, D. J. Priour, Jr., B. Wang, and S. Das Sarma, Phys. Rev. B **83**, 075105 (2011).
[7] M. Wilkinson, Proc. R. Soc. Lond. A **391**, 305 (1984); See also: Y. Zhang, D. Bulmsh, A. V. Maharaj, C.-M. Jian, and S. A. Kivelson, arXiv:1504.05205 (2015).
[8] Y. Wang, G. Xianlong, and S. Chen, Eur. Phys. J. B **90**, 215 (2017).
[9] S. Aubry and G. André, Ann. Israel Phys. Soc. **3**, 18 (1980).
[10] P. G. Harper, Proc. Phys. Soc. A **68**, 874 (1955).
[11] D. R. Hofstadter, Phys. Rev. B **14**, 2239 (1976).
[12] C. Aulbach, A. Wobst, G.-L. Ingold, P. Hänggi, and I. Varga, New J. Phys. **6**, 70 (2004).
[13] Y. E. Kraus, Y. Lahini, Z. Ringel, M. Verbin, and O. Zilberberg, Phys. Rev. Lett. **109**, 106402 (2012).
[14] L.-J. Lang, X. Cai, and S. Chen, Phys. Rev. Lett. **108**, 220401 (2012).
[15] Y. E. Kraus and O. Zilberberg, Phys. Rev. Lett. **109**, 116404 (2012).
[16] W. P. Su, J. R. Schrieffer, and A. J. Heeger, Phys. Rev. Lett. **42**, 1698 (1979).
[17] R. Wakatsuki, M. Ezawa, Y. Tanaka, and N. Nagaosa, Phys. Rev. B **90**, 014505 (2014).
[18] A. Y. Kitaev, Phys.-Usp. **44**, 131 (2001).
[19] Q. B. Zeng, S. Chen, and R. Lü, Phys. Rev. B **94**, 125408 (2016).
[20] D. J. Thouless, Phys. Rev. Lett. **61**, 2141 (1988).
[21] S. Das Sarma, S. He, and X. C. Xie, Phys. Rev. Lett. **61**, 2144 (1988).
[22] J. Biddle and S. Das Sarma, Phys. Rev. Lett. **104**, 070601 (2010).
[23] T. Liu, P. Wang, S. Chen, and G. Xianlong, J. Phys. B: At., Mol., Opt. Phys. **51**, 025301 (2018).
[24] J. C. C. Cestari, A. Foerster, and M. A. Gusmão, Phys. Rev. B **93**, 205441 (2016).
[25] F. Liu, S. Ghosh, and Y. D. Chong, Phys. Rev. B **91**, 014108 (2015).
[26] S. Ganeshan, K. Sun, and S. Das Sarma, Phys. Rev. Lett. **110**, 180403 (2013).
[27] G. Roati, C. D'Errico, L. Fallani, M. Fattori, C. Fort, M. Zaccanti, G. Modugno, M. Modugno, and M. Inguscio, Nature (London) **453**, 895 (2008).
[28] J. Chabé, G. Lemarié, B. Grémaud, D. Delande, P. Szriftgiser, and J. C. Garreau, Phys. Rev. Lett. **101**, 255702 (2008).
[29] L. Dal Negro, C. J. Oton, Z. Gaburro, L. Pavesi, P. Johnson, A. Lagendijk, R. Righini, M. Colocci, and D. S. Wiersma, Phys. Rev. Lett. **90**, 055501 (2003).
[30] Y. Lahini, R. Pugatch, F. Pozzi, M. Sorel, R. Morandotti, N. Davidson, and Y. Silberberg, Phys. Rev. Lett. **103**, 013901 (2009).
[31] X. Cai, L.-J. Lang, S. Chen, and Y. Wang, Phys. Rev. Lett. **110**, 176403 (2013).
[32] H. Hiramoto and M. Kohmoto, Phys. Rev. B **40**, 8225 (1989).
[33] J. H. Han, D. J. Thouless, H. Hiramoto, and M. Kohmoto, Phys. Rev. B **50**, 11365 (1994).
[34] A. Altland and M. R. Zirnbauer, Phys. Rev. B **55**, 1142 (1997).
[35] E. Lieb, T. Schultz, and D. Mattis, Ann. Phys. (N.Y.) **16**, 407 (1961).
[36] P. G. de Gennes, *Superconductivity of Metals and Alloys* (Benjamin, New York, 1966).
[37] J. Wang, X.-J. Liu, G. Xianlong, and H. Hu, Phys. Rev. B **93**, 104504 (2016).
[38] D. J. Thouless, J. Phys. C: Solid State Phys. **5**, 77 (1972).
[39] M. Kohmoto, Phys. Rev. Lett. **51**, 1198 (1983).
[40] M. Kohmoto and D. Tobe, Phys. Rev. B **77**, 134204 (2008).
[41] J. E. Avron, R. Seiler, and B. Simon, Phys. Rev. Lett. **51**, 51 (1983).
[42] P. Středa, J. Phys. C **15**, L717 (1982).
[43] R. O. Umucalilar, H. Zhai, and M. Ö. Oktel, Phys. Rev. Lett. **100**, 070402 (2008).